Research paper

TecPIV—A MATLAB-based application for PIV-analysis of experimental tectonics

D. Boutelier

School of Environmental and Life Sciences, University of Newcastle, University Drive, Callaghan 2308, NSW, Australia

ABSTRACT

TecPIV is a MATLAB-based, open source application aiming to facilitate and accelerate the Particle Image Velocimetry (PIV) analysis of analogue tectonic models. Since tectonic modelling experiments are usually slow, low sensitivity but high resolution digital cameras can be employed to monitor displacements and calculate strain from PIV analysis. The presented work-flow package provides an integrated environment to import raw files, calibrate, enhance, undistort and rectify the views of the model, calculate the incremental displacements between successive images, the spatial derivatives, and the Eulerian cumulative displacements. The calibration procedure employs a combination of linear and polynomial functions allowing correction of both lens and parallax distortions. The cross-correlation uses a parallelized FFT-method to accelerate the processing of large images. The performance is tested using synthetic images designed to evaluate the precision of the produced velocity field for various settings as well as the ability to capture sharp features characteristic of experimental tectonics.

© 2016 Elsevier Ltd. All rights reserved.

1. Introduction

The concept of similar systems rests on the idea that multiple physical systems may share the same underpinning physics and therefore one can draw inferences from observations in any of the similar systems. The concept can be traced back to famous seventeenth century physicists Galileo and Newton (Sterrett, 2009, and reference therein).

In Earth sciences, scaled models have been employed for over a century to test hypotheses on the driving mechanisms of tectonic processes derived from and constrained by a variety of geological and geophysical data (Koyi, 1997; Ranalli, 2001; Graveleau et al., 2012, and reference therein). The scaled model passes through an evolution which simulates that of the original, but on a much more convenient scale (e.g. Buckingham, 1914; Hubbert, 1937; Ramberg, 1967). The process can thus be precisely monitored in time and space, thereby allowing its dynamics to be investigated.

However, to unravel the physics of the investigated process, its evolution (in space and time) must not only be recorded but also quantified. In fluid dynamics experiments, the fluid whose flow needs to be quantified is seeded with tracers and time-lapse photographs are employed to derive the flow field using an image correlation technique (e.g. Lourenco et al., 1989; Willert and Gharib, 1991; Adrian, 1991). This technique, called Particle Imaging Velocimetry (PIV) technique, has been also employed for tectonic laboratory experiments where the displacements of sand grains or other passive markers are quantified and strain or strain-rate components are derived allowing precise measurement of where, how, and when deformation occurs in the model (e.g. Adam et al., 2005; Schrank et al., 2008; Le Corvec and Walter, 2009; Leever et al., 2011).

Because commercial PIV systems are primarily designed for the quantification of rapid fluid flow, these systems usually employ expensive, high sensitivity but relatively low resolution digital cameras (<10 Mpixels). The high sensitivity is required to capture the rapid motion of the tracers in the fast-moving fluid at high frequency. The low-resolution is a consequence of the required high frequency because it remains technically challenging to move or store a large quantity of large images at high rates. However, many analogue modelling experiments of tectonics are produced at very low rates (i.e. ≪1 mm s^{-1}) (e.g. Corti et al., 2003) or are not rate-sensitive at all and therefore the rate can be set as low as desired (e.g. Hoth et al., 2007). Therefore lower sampling rates can be used, allowing the use of less expensive, higher resolution (up to 50 Mpixels) consumer grade digital cameras (DSLR) to capture sufficient light during longer exposure time.

Here we present an integrated work-flow software designed to facilitate and accelerate the PIV analysis of large images from such DSLRs. The objectives are to provide a reasonably easy way to

E-mail address: david.boutelier@newcastle.edu.au

import raw files, calibrate, enhance, undistort and rectify the views, calculate the incremental displacements, the spatial derivatives and the Eulerian cumulative displacements via one single graphical user interface.

We present the methods, and benchmark the software using synthetic images. The code is available at https://bitbucket.org/david_boutelier/tecpiv and has been developed on and tested with Microsoft® Windows® 7 and MATLAB® 2014b. Videos demonstrating the use of the software are available at https://www.youtube.com/user/dboutelier/videos.

2. PIV principles

In fluid dynamics experiments monitored with PIV, a plane within the fluid is illuminated using a laser sheet and the light scattered by the particles is recorded on two successive images (e.g. Adrian, 1991). Each image is then divided into small interrogation areas and the local displacement vector between the two images is determined for each interrogation area by cross-correlation (Fig. 1). The algorithm calculates the shift for which each interrogation window best matches the next image. Given the
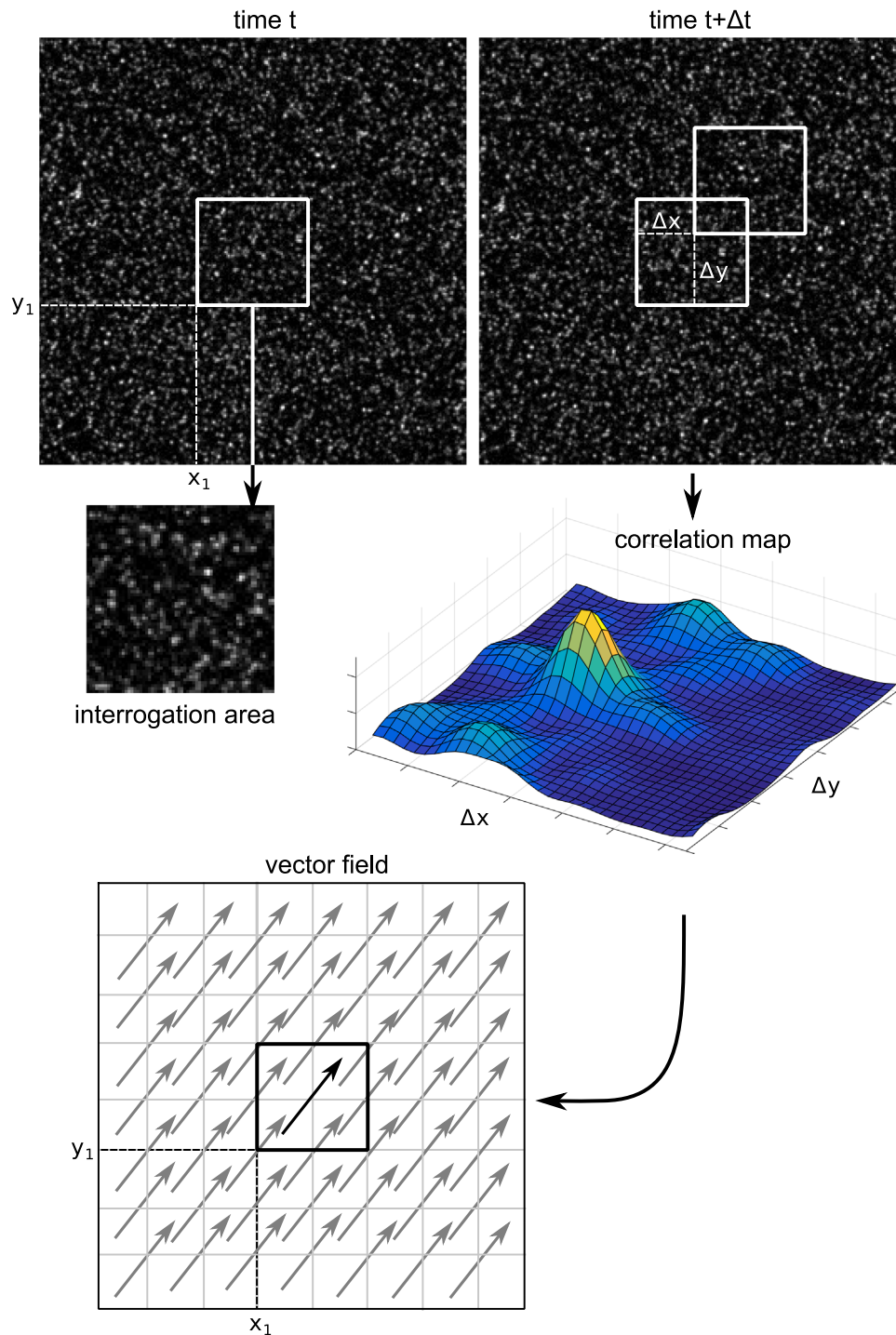

Fig. 1. Illustration of the principles of Particle Imaging Velocimetry. Two images are correlated at time t and $t + \Delta t$. An interrogation window from image at time t is correlated with the image at time $t + \Delta t$. The correlation is a map in the space defined by the shifts in the x and y directions. The position of the peak provides the displacement of the interrogation window between time Δt.
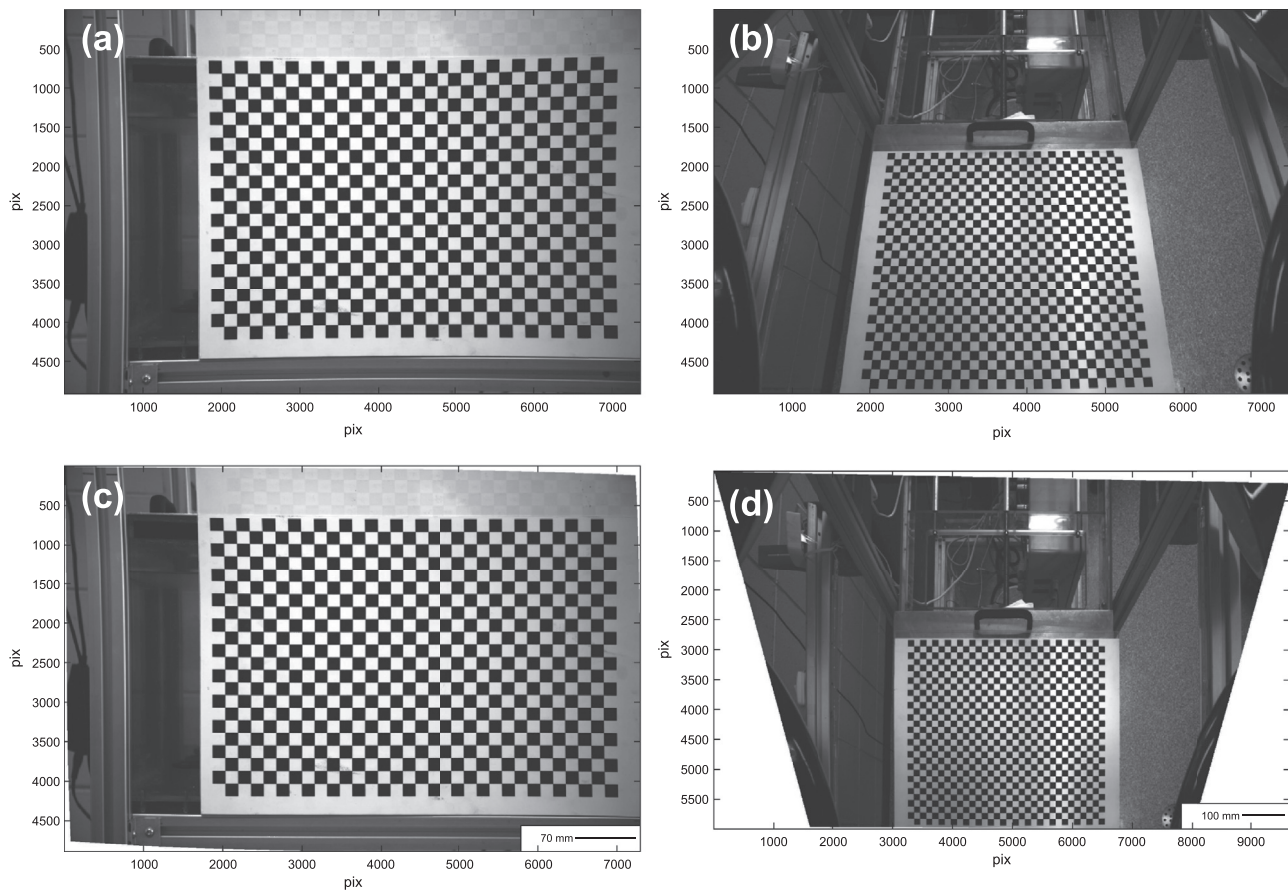
Fig. 2. Calibration and rectification of 2 views of a calibration board. (a) Original side view. The view is approximately perpendicular to the plane of the board placed against the side of the experimental apparatus. The employed wide-angle lens produced a strong cushioning distortion. (b) Original surface view with significant obliquity requiring a combination of linear and polynomial corrections. The board is placed horizontally on top of the experimental apparatus. The vertical distance between the model surface to monitor and top of the calibration board is measured and the camera is lowered by this value before the start of the experiment. (c) Corrected side view using a degree-3 polynomial function. (d) Corrected surface view.

time interval between the two images and the image scaling, the local flow velocity vector (i.e. in real world units) can be deduced.

3. PIV workflow

3.1. Project structure

We define an experimental dataset as one or more images of a calibration board with a specific and known geometrical pattern, and a series of images of the analogue model during deformation, from the same camera, in the same position, with the same settings. The images are taken using the raw format, which includes the entire data from the image sensor without any processing but with numerous meta-data regarding the settings of the camera. The images in raw format must be converted to DNG (Digital Negative), an open raw format, and archived. Each project created within the software package TecPIV can import the DNG files and convert them to 16-bit greyscale tiff. This procedure allows abstracting the specifications of the camera, since they are taken care of by the free DNG converter (e.g. Adobe®), outside of our project. Furthermore, archiving in the open DNG format means that the raw data is preserved, including color information and meta-data, in a documented, perennial format.

3.2. Preprocessing

Preprocessing serves to establish a relationship between the

displacement of the interrogation area, in pixels between correlated frames, and the real displacement rate in the real world, in physical dimensions. At it simplest, the task would be assigning a scaling factor and sampling frequency. However experimental images are usually not perfect and a unique scale factor cannot be employed without first removing the distortions in the image.

Our experimental apparatus uses a remote to trigger the cameras at a constant frequency, therefore the time interval is not considered an issue here. We simply provide the employed time interval.

3.2.1. Image calibration

There are two main types of image distortion that must be corrected prior to correlation. The image may include distortions due to the imperfection of the lens leading to non-linear barrel, or cushioning distortion. The view of the model may also be oblique, thereby inducing perspective and linear spatial variations of the image scale (Jenkins and White, 1957).

There are two main procedures that can be used to remove the distortions. A camera model can be constructed using a number of views of a known geometrical pattern (Zhang and Way, 1999). This allows calculating the intrinsic and extrinsic characteristics of the camera, which control the lens and perspective distortions respectively. Once the camera parameters are estimated it is possible to remove the distortions.

Another solution is to transform the image using linear or polynomial functions such that control points in one single calibration image align with the known relative positions of these

points in the physical world (Pawlowicz, 2003). The advantage of the camera model procedure lies in that the constraints from the control points on a number of calibration images permit the correction of the distortion everywhere in the image space, whereas the linear/polynomial transformation only allows correction within the subspace defined by the control points. The advantage of the linear/polynomial transformation is that the procedure requires only one single view of a known geometrical pattern.

We employ the linear/polynomial transformation method using one view of a checkerboard pattern. The Harris corner detector (Harris and Stephens, 1988) implemented in the MATLAB ® Camera Calibration Toolbox (http://www.vision.caltech.edu/bouguetj/calib_doc/) is employed to estimate the image coordinates of control points with sub-pixel precision. The number of squares along the X- and Y-axes and the physical size of the squares are employed together with the averaged image scale at the centre of the calibration board to define the target position of the control points: the positions they should be at in order to have a regular grid with a homogeneous image scale. A simple linear function or a polynomial function of degree 2–4 can be employed.

For oblique views, we use a two steps combination of linear transformation to remove the linear distortion due to obliquity, and polynomial to remove the non-linear distortion due to the imperfection of the lens. The error on the removal of distortion is estimated (2σ), allowing the various options (linear transformation, or polynomial degree 2–4, or combination of linear plus polynomial) to be tested successively and the best strategy (i.e. lowest error) to be determined.

Fig. 2 shows two views of an experimental apparatus. The first view (Fig. 2a) is approximately perpendicular to the side of the experimental apparatus. It displays a calibration board with 651 control points defined by 15 mm black and white squares. The resolution at the centre of the calibration board is 10.89 pixels/mm. A degree-3 polynomial function was used to transform the coordinates of the control points to their target positions (Fig. 2c). The difference between the coordinate of the transformed control point and its target position is calculated for each control point and the error (2σ) is calculated for the X- and Y-axis. Here the errors are 0.69 and 0.72 pixels amounting to 0.064 mm for a calibrated area of 450×300 mm.

The second model view, from above, is oblique (Fig. 2b) and therefore needs more correction. This is performed using the two-steps method. The calibration board displays 899 control points defined by the same 15 mm black and white squares. The resolution at the centre of the calibration board is 6.7 pixels/mm. The first step uses a direct projection method which yields errors of 12.35 and 13.28 pixels for the X- and Y-axes respectively, confirming that the view also includes severe non-linear distortion due to the employed wide-angle lens. The second step (Fig. 2d) using a degree 3 polynomial function reduces the error to 1.8 and 2.1 pixels for the X- and Y-axes respectively, which amount to ~0.3 mm for a calibrated area of 450×430 mm.

The correction function is then employed to correct the entire experimental dataset. The processing time increases linearly with the size of the dataset but the rate also varies with the employed method (Fig. 3a). It is faster to employ a linear function than a polynomial function. The degree of the polynomial function does not influence significantly the processing time, but using a combination of linear and polynomial functions severely increases the computation time (Fig. 3a).

Since the task of applying the calculated correction function to a dataset containing several hundred images is embarrassingly parallel, the task is accelerated using the MATLAB parallel computing toolbox (Fig. 3b).
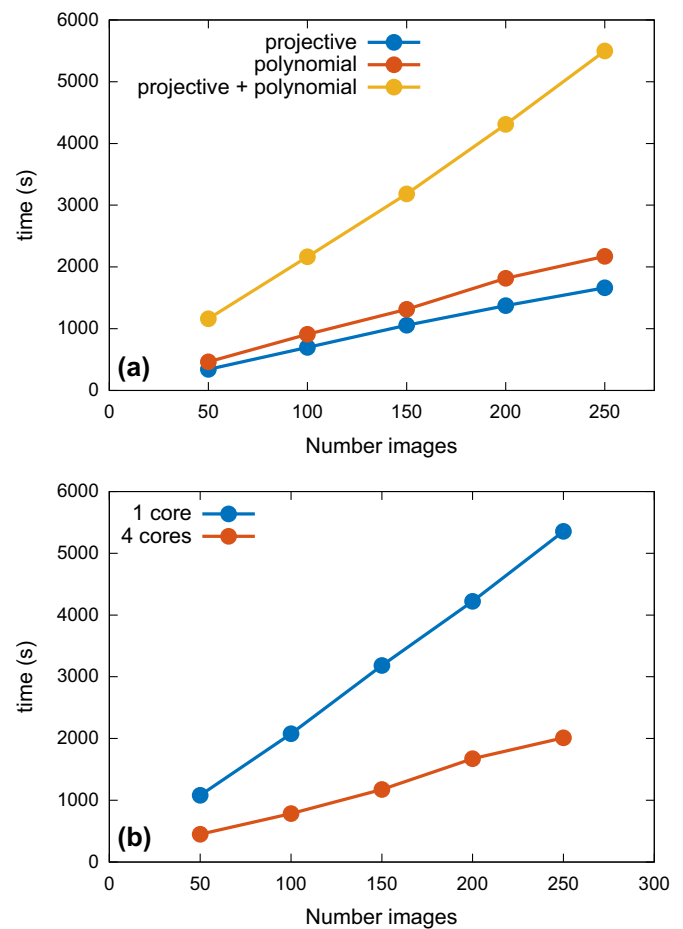

Fig. 3. Correction of 36 Mpixels images. (a) Various correction methods employed with a 4 cores computer. The projective function gave an error (2σ) of ~15 pixels, while the polynomial functions of degree 2 and 3 gave errors of ~5 and ~12 pixels respectively. The use of both projective and polynomial functions reduced the error to ~2 pixels at the expense of calculation time. (b) Corrections of the same images using a polynomial function of degree 3 for execution on 1 or 4 cores computer.

3.2.2. Image enhancement

Preprocessing also aims at making the experimental images more suitable for the correlation procedure. The images need to have a pattern with sufficient contrast between the particles and background such that it can be reasonably assumed that each interrogation area possesses a unique distribution of values. To that aim, the distribution of intensities is adjusted by first inverting the image, subtracting a local background value calculated using a Gaussian filter, and normalizing the intensities (Fig. 4).

To minimize storage space, pre-processing of the image is done as a first step in the image correlation, not a separate procedure. Before two images are cross-correlated, the contrast enhancement procedure is applied to each. The enhanced images are employed for the cross-correlation but not stored.

3.3. Image correlation

3.3.1. Single pass

The FFT (Fast Fourier Transform) algorithm is used to transform the sub-areas of two successive images into the frequency domain (Smith, 1999). Multiplying the real and imaginary parts of the first image I_1 with the real and imaginary parts of the second image I_2 generates the real and imaginary parts of the correlation map in the frequency domain. The Inverse FFT completes the operation and yields the correlation map C in the spatial domain, where the value of each pixel is the measure of how well the two images
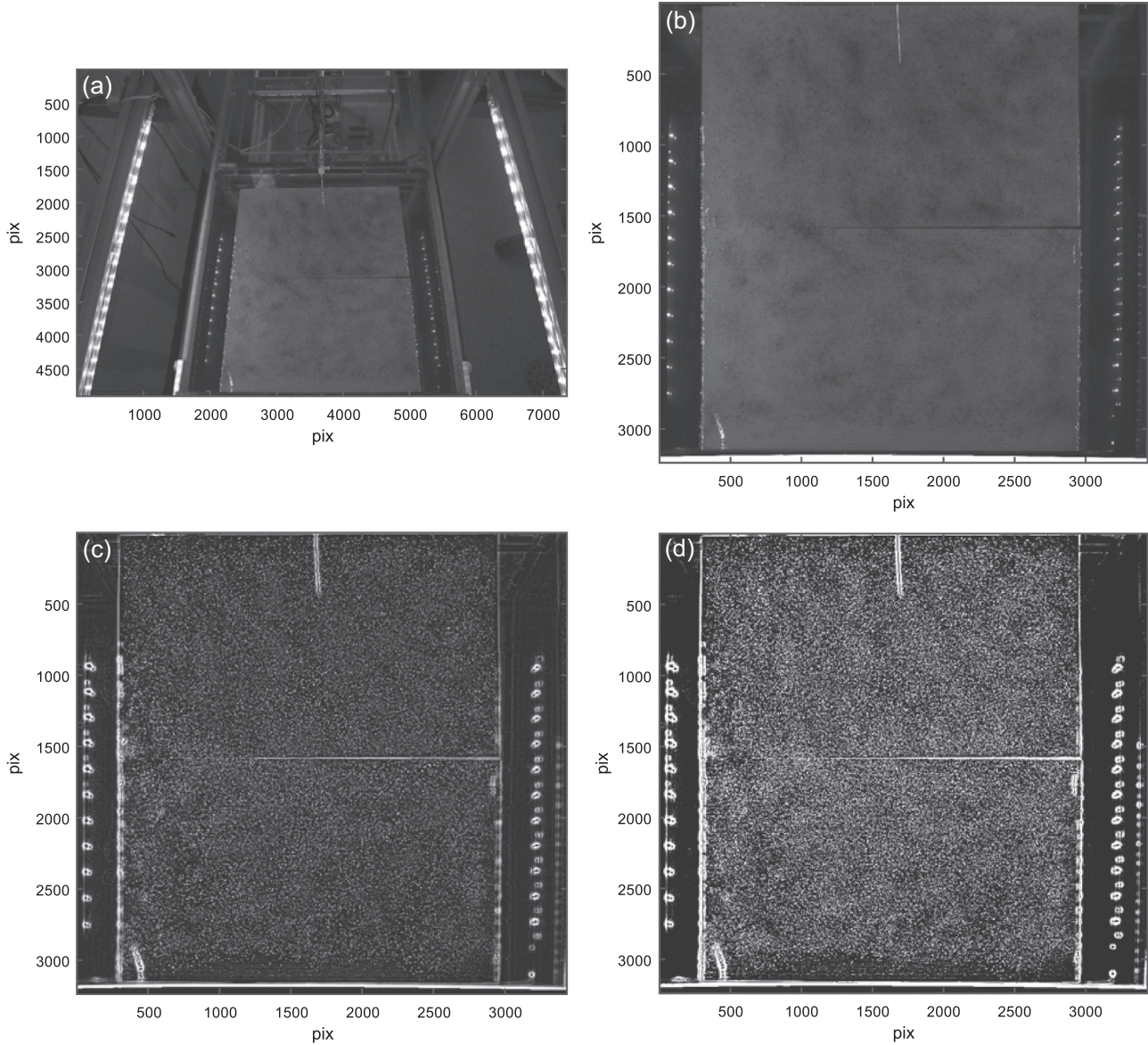
Fig. 4. Example of image enhancement before cross-correlation. (a) Original oblique surface view of an analogue model with dark particles sifted on model surface to create a unique distribution of values. (b) rectified and cropped surface view. (c) Same view with intensities inverted and background removed using a Gaussian filter (window size 100 pixels and Gaussian σ 10 pixels). (d) Same view with intensities normalized.

match when shifted by the coordinates of the point (Smith, 1999). Correlating an image with itself thus yields a peak at the origin, while correlating two identical but shifted images yields a peak located at the shift vector:

$$C(x, y) = \mathcal{F}^{-1}\{\mathcal{F}\{I_1(x, y)\} \times \mathcal{F}\{I_2(x, y)\}\} \tag{1}$$

where $\mathcal{F}$ is the FFT operator. To strengthen the calculation of the displacement vector, only the peaks with a signal to noise ratio greater than a critical value are kept. The signal to noise ratio is defined as

$$SNR = \frac{\max(C) - \bar{C}}{\sigma(C)} \tag{2}$$

with

$$\sigma(C) = \sqrt{\frac{1}{N} \sum_{i=1}^{N} \left(C_i - \bar{C}\right)^2} \tag{3}$$

Since each correlation of a pair of interrogation windows yields

one single vector and the operation needs to be repeated numerous times for each image pair, the parallelization can be set at the level of the interrogation area. This means that the image pairs are processed sequentially, using for each pair all the available cores. This provides the opportunity to update the region of interest using the calculated vector field before processing the next image pair.

The implementation of the FFT correlation is a modification of that provided in the open source PIV project, PIVLab (Thielicke and Stamhuis, 2014). We parallelized Thielicke and Stamhuis (2014) algorithm in order to accelerate the procedure for large images and implemented the calculation of signal to noise ratio, validation of the peak as well as the deforming mask. The performance of the parallelization is further explored in Section 4.

3.3.2. Multipass

A large interrogation window yields a better likelihood of unique distribution of values and therefore a more robust correlation (Raffel et al., 2007). However, it may also require more
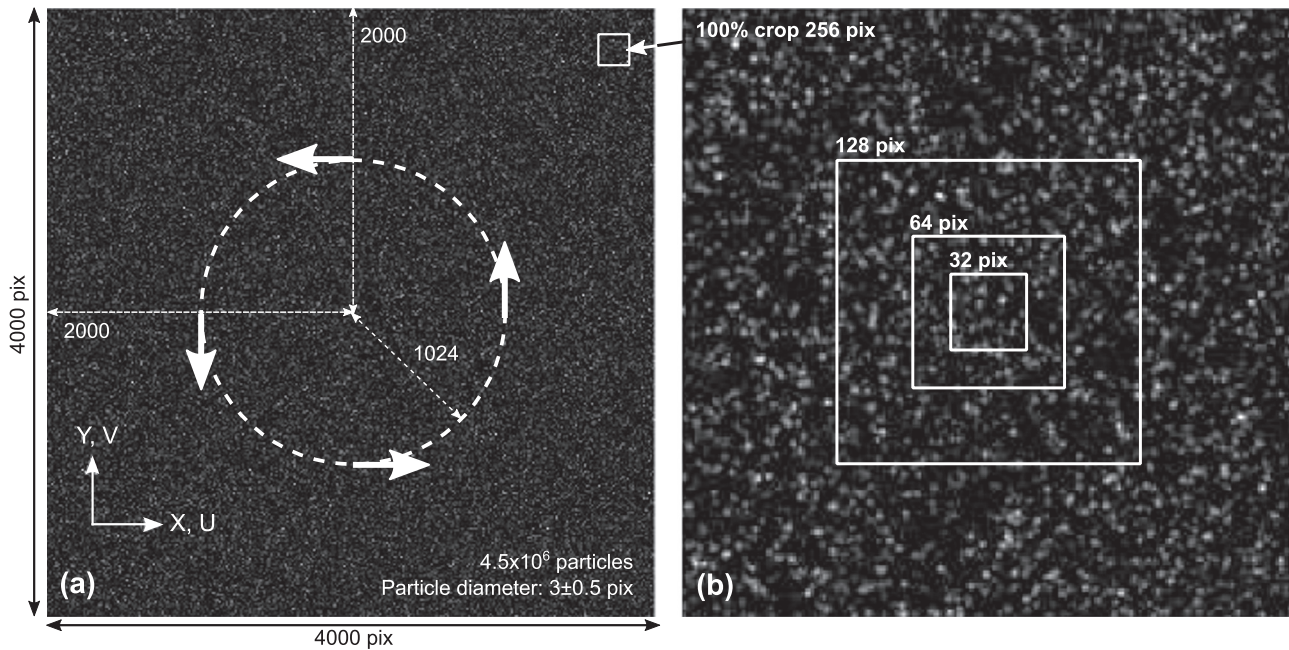
Fig. 5. Setup of the Rankine vortex synthetic tests. A vortex with radius of 1024 pixels is centred at $X=2000$ and $Y=2000$ pixels. The velocity is 5 pixels, decreasing linearly towards the centre of the vortex and non-linearly outside. The synthetic images are 4000×4000 pixels. The particle density is $\rho_p = 2.8 \times 10^{-2}$ pixels^{-2} and particle diameter is 3 ± 0.5 pixels. The images are correlated using interrogation windows 256 to 32 pixels and various amount of overlap. (a) Full synthetic image with position of the vortex. (b) 100% Crop with squares corresponding to interrogation areas 256 to 32 pixels.

computation power and unless a large overlap between successive interrogation windows is specified, it will generate a coarse vector grid which may not be able to resolve the physical process (e.g. a narrow fault). A multipass approach provides the ability to calculate a dense vector field through the use of interrogation window sizes that progressively reduce in each pass. The result of each pass is used to shift the interrogation windows during the next pass, thereby increasing resolution without sacrificing robustness (Raffel et al., 2007).

Our algorithm allows the use of up to four successive passes with decreasing interrogation window size and accordingly increasing resolution of the resulting grid. However contrary to the original algorithm of Thielicke and Stamhuis (2014), the interrogation areas are not deformed. This feature was removed to facilitate the parallelization. The performance of the multipass approach is further explored in Section 4.

3.3.3. Sub-pixel displacement

As actual displacements do not necessarily correspond to pixel-size increments, an accurate estimate of the displacement field requires a resolution below the pixel limit. A widely used method to derive the sub-pixel displacement is to fit a Gaussian function to the correlation map to measure more precisely the position of the maximum. The Gaussian fit can be obtained using a simple 3-point estimator following the work of Uri Shavit, Roi Gurka and Alex Liberzon in URAPIV (Taylor et al., 2010), now OpenPIV (www.openpiv.net) or a more complex 2D Gauss regression following Nobach and Honkanen (2005).

3.4. Post-processing

The vector field for each image pair is evaluated using a number of filters and some vectors are discarded, and recalculated using an interpolation scheme.

3.4.1. Displacement filtering

The simplest way to filter the vectors is to compare the X and Y component of the displacement D (in pixel) to set minimum and maximum values:

$$\min \; < D_x | D_y < \; \max \tag{4}$$

3.4.2. Standard deviation filtering

The standard deviation is calculated for the entire vector field and the vector is validated if the difference between the displacement vector D_i and the mean $\bar{D}_i$ is inferior to a set threshold K multiplied by the standard deviation σ. By default, K is set to 2:

$$D_i - \bar{D}_i < K\sigma \tag{5}$$

where D_i ($i = x, y$) is the component of the displacement vector in the reference frame.

3.4.3. Universal outliers filtering

A popular filtering method for detection of spurious vectors is the *universal outliers* detection algorithm of Westerweel and Scarano (2005), which normalizes the residual r of the displacement D of one data point relative to the median $\tilde{D}$ of its nearest neighbours, by the local median of the residuals of each neighbour $\tilde{r}$, taking into account a tolerance ϵ associated with the noise of the data:

$$r = \frac{|D - \tilde{D}|}{\tilde{r} + \epsilon} < K_u \tag{6}$$

This filter has been shown to allow the data points in high-gradient areas to not be considered outliers simply due to the variability of their neighbours (Westerweel and Scarano, 2005).

3.4.4. Interpolation

Vectors that do not meet the criteria associated with the employed filters are set to NaN and may be interpolated using various options. Following PIVlab, a boundary value solver is employed (Thielicke and Stamhuis, 2014). A partial differential equation (PDE) is formulated and the perimeter of the hole in the data supplies the boundary values for the PDE, approximated
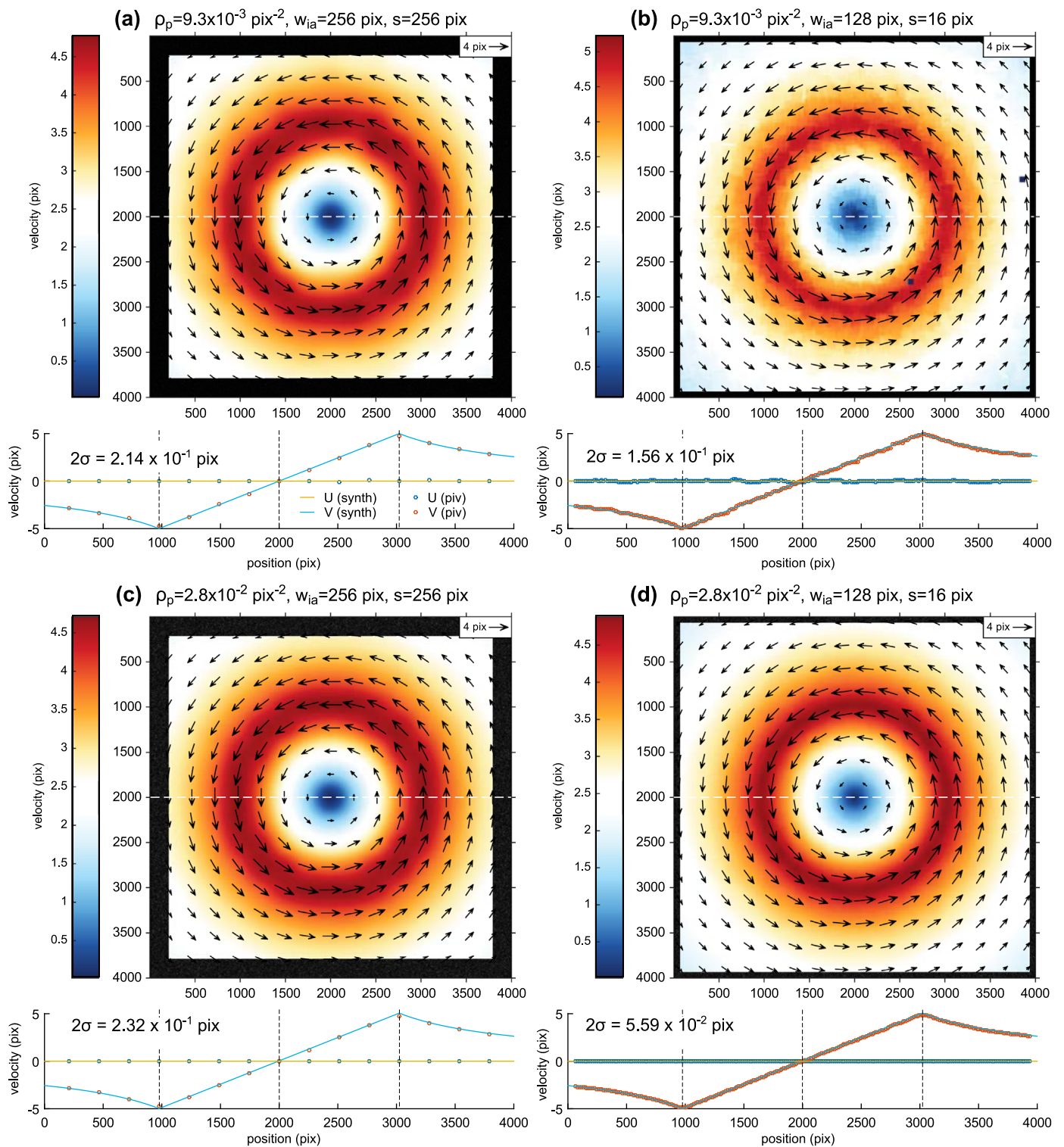
Fig. 6. Comparison of Rankine vortex synthetic tests. Profiles are produced along line $Y=2000$. The imposed flow is represented by the solid lines while the measured vectors are the points. Error is 2σ. Particle density ρ_p is calculated by dividing the number of particles by the surface area of the image in pixel-squared. The employed particles are 3 ± 0.5 pixels in diameter. w_{ia} is the size of the interrogation area and s is the resolution of the vector grid.

using finite difference methods. A variety of differential equation models can be specify to be solved.[1] The performance of the

interpolator for various amount of missing data has been tested by Thielicke and Stamhuis (2014).

3.5. Spatial derivatives

To facilitate the analysis, it is common to drape the velocity or displacement vectors and some spatial derivatives on the view of

---

[1] The interpolation algorithm and its description can be obtained at http://au.mathworks.com/matlabcentral/fileexchange/4551-inpaint-nans/content/Inpaint_nans/doc/methods_of_inpaint_nans.m
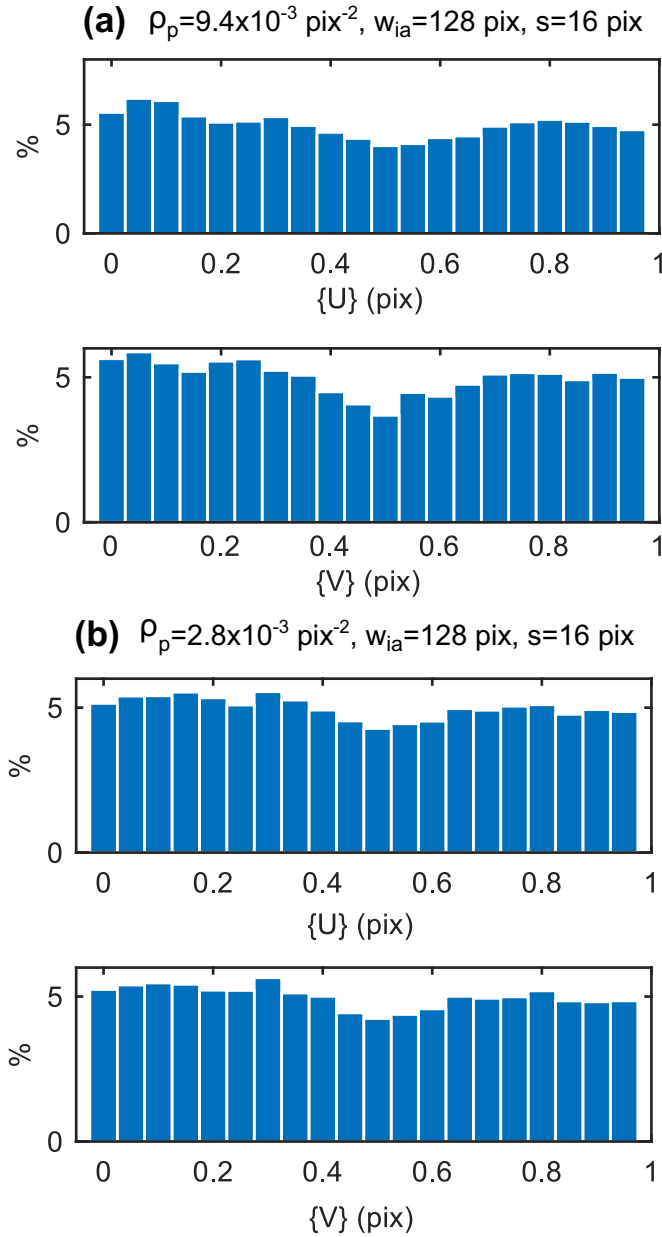
(a) $\rho_p = 9.4 \times 10^{-3}$ pix^{-2}, $w_{ia} = 128$ pix, $s = 16$ pix

(b) $\rho_p = 2.8 \times 10^{-3}$ pix^{-2}, $w_{ia} = 128$ pix, $s = 16$ pix

Fig. 7. Histograms of the decimal parts of the velocity components U and V for the Rankine vortex presented in Fig. 6(b) and (d). The absence of peak at 0 indicate good sub-pixel measurement of displacement. The Rankine vortex processed with large interrogation window and no overlap (Fig. 6(a) and (c)) provided too few vectors to conclude statistically about the presence or absence of peak locking.
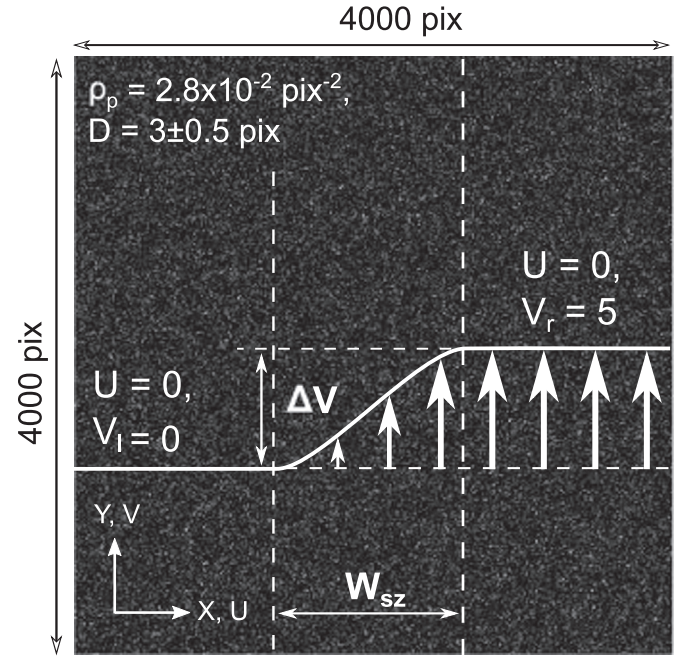

Fig. 8. Set-up of shear zone synthetic tests. The centre and width the shear zone is defined as well as the outside velocities. In the shear zone V varies following the error function (erf). Therefore the shear strain across the shear zone is a Gaussian curve. Series of 300 successive images have been created to calculate large cumulative displacements. $V_l = 0$ on the left side of shear zone and $V_r = 5$ on the right side of shear zone.

$$w = \left(\frac{\Delta D_x}{\Delta y \Delta t} - \frac{\Delta D_y}{\Delta x \Delta t} \right) \tag{8}$$

and divergence:

$$\nabla \cdot V = \left(\frac{\Delta D_x}{\Delta x \Delta t} + \frac{\Delta D_y}{\Delta y \Delta t} \right) \tag{9}$$

Although the colouring is generally employed for the spatial derivatives, it can also be used to display the spatial distribution of the magnitude or azimuth of the displacement vectors, or their X and Y components.

4. Synthetic tests

The synthetic images are generated using a known displacement field. The PIV algorithm is then employed on the pair or more of synthetic images and a vector field is derived for each image pair. The test is successful when the key characteristics of the imposed flow can be retrieved.

4.1. Rankine vortex

A circular flow is imposed at a known distance from a precisely known centre point (Fig. 5). Within the vortex the velocity increases linearly with the distance from the centre. Outside of the vortex, the magnitude of the velocity decreases with the inverse of the distance to the vortex.

The images are 4000 by 4000 pixels. The vortex is centred at 2000 and 2000 pixels, the radius of the vortex is 1024 pixels and the maximum incremental displacement is 5 pixels. Up to 4.5×10^5 particles with a mean diameter of 3 ± 0.5 pixels are advected. The particle density is therefore $\rho_p = 2.8 \times 10^{-2}$ pixels^{-2}. The PIV analysis is performed using various sizes of the interrogation area w_{ia} and resolution s of the produced vector grid.

the deformed model (e.g. Boutelier and Oncken, 2011). The displacement is represented by a field of vectors while the chosen spatial derivative is represented by semi-transparent colors on top of the greyscale model view.

The strain-rate components are defined as

$$\dot{E}_{ij} = \frac{\Delta D_i}{\Delta j \Delta t} \tag{7}$$

where D is the displacement, i and j are the X or Y coordinate axes, and t is the time.

Combinations of strain derivatives are calculated such as the vorticity w:
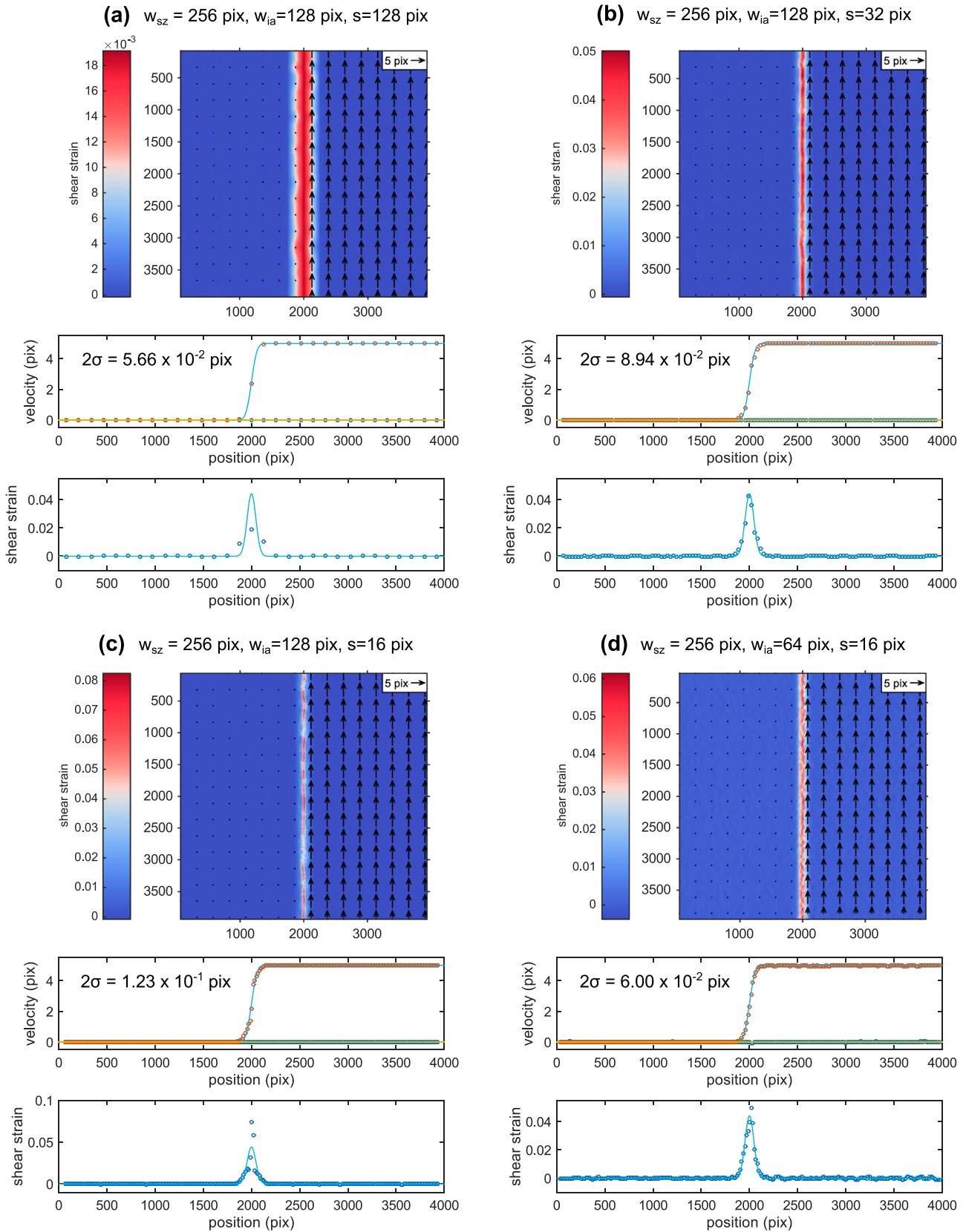
Fig. 9. Comparison of displacement vector map and profiles across a narrow synthetic shear zone ($W_{sz} = 256$ pixels) with different PIV settings. (a) Overlap 0%. Although the error on displacement is small, the shear strain profile derived from PIV is too wide and its peak is too low. (b) Overlap 75%. Higher number of vectors provides a better capture of strain distribution in the shear zone. (c) Overlap 87.5%. Excessive overlap leads to discontinuous movement (fault). Shear strain profile is not Gaussian and its peak is overestimated. (d) Overlap 75%. Highest resolution on shear distribution is achieved using reasonable overlap with smallest interrogation area providing reasonable noise (here 64 pixels, with particle density of 2.8×10^{-2} particle/pixels^2).
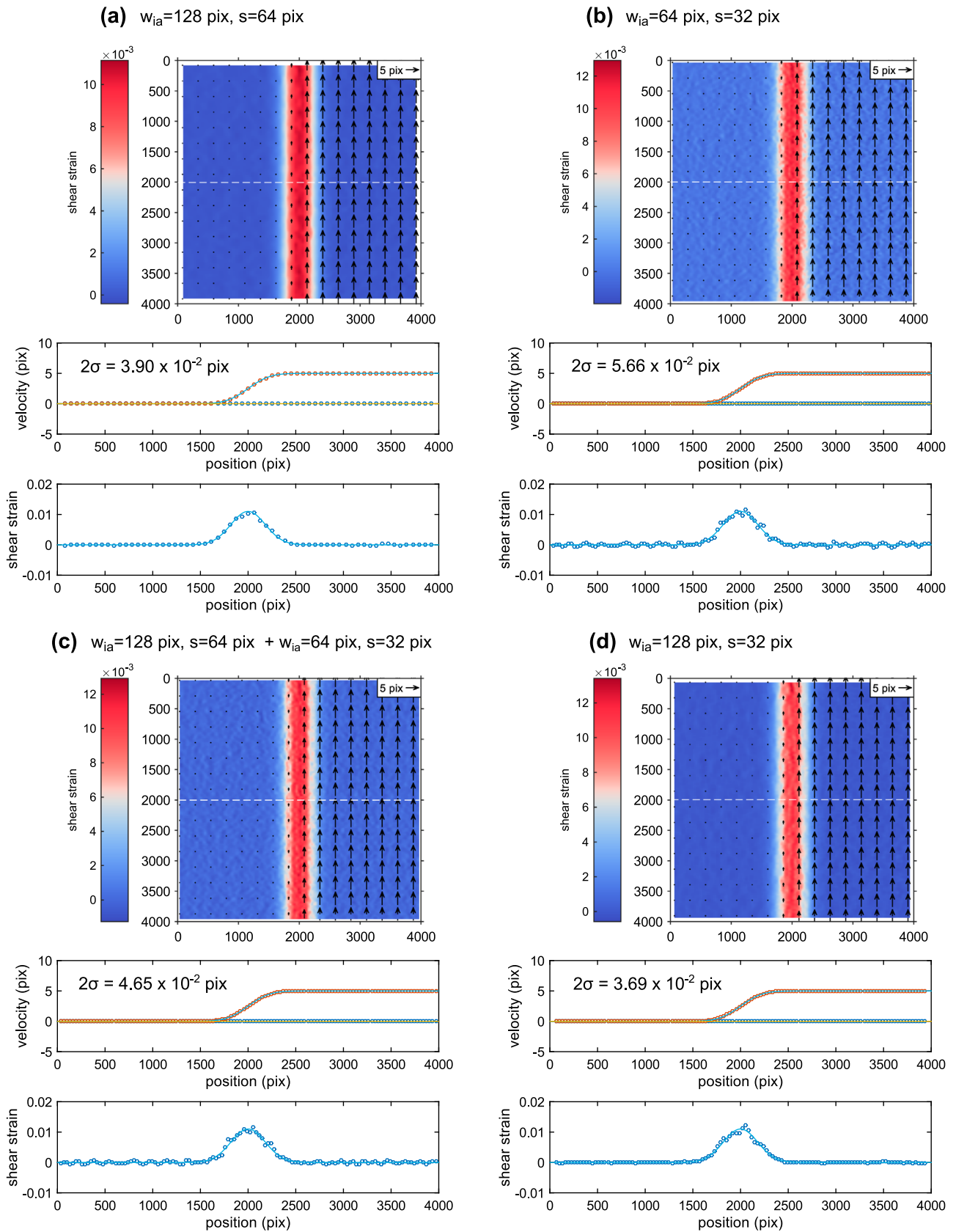
Fig. 10. Multipass vs. overlap strategies. $w_{sz} = 1024$ pixels, $V_r = 5$, $V_l = 0$ pixels. $\rho_p = 2.8 \times 10^{-2}$ pixels^{-2}. (a) Single pass $W_{ia} = 128$ pixels, $s = 64$ pixels. The large window size provides low noise and good accuracy, but limited number of datapoints within the shear zone. (b) Single pass $W_{ia} = 64$ pixels, $s = 32$ pixels. The smaller window size allows calculation of many more vectors but the noise increases. (c) Multipass, $W_{ia} = 128$ pixels, $s = 64$ followed by $W_{ia} = 64$ pixels, $s = 32$ pixels. The resolution is high (vector every 32 pixels) and noise decreased compared to single pass with equivalent last pass settings. (d) Single pass with large window size and slightly larger overlap. Overlap is increased to 75% which yields vector grid resolution of 32. If the shear zone is not too narrow then increasing the overlap provides best resolution together with lowest noise.

We extracted velocity profiles passing though the centre of the vortex and parallel to the *X*-axis (Fig. 6). All the profiles captured the essence of the vortex: the position of the centre, the sense of movement as well as the position of the maximum velocity, linear decrease inside the vortex and non-linear outside (Fig. 6).

A smaller interrogation area (128), combined with large overlap (87.5%), yield maps with many more vectors, able to resolve small spatial variations (Fig. 6b, d), however the small interrogation area yields significantly more noisy profile when the particle density decreases (Fig. 6b, d). A larger interrogation window thus provides a way to obtain a good signal despite a low particle density albeit with lower resolution (Fig. 6a, c).

We further employed the Rankine test to investigate if the velocity vectors lock on integer values. To this end, the integer part of the velocity component is removed. If peak locking occurs, the distribution of the decimal parts will yield peaks at 0. Fig. 7 reveals that this is not the case.

The good agreement between imposed and measured velocity gradient, low error and absence of peak locking indicates that for window size of about 128 pixels and with significant amount of overlap (50–75%) the measure of displacement is very accurate and the precision on the displacement is sub-pixel. However, if the window size is too small, noise may appear if the particle density is too low. Increasing the window size does reduce the error and noise, and allows capturing the characteristics of the flow, but the produced vector grid is coarse.

4.2. Shear zone

In order to be most useful to the analysis of analogue models of tectonics, it is important to test the ability of the algorithm to capture sharp features and large cumulative displacements. As in the example above, a series of images is created using a known velocity field to advect the particles. The images are 4000 by 4000 pixels, the particle density is up to 2.8×10^{-2} pixels^{-2} and the particle diameter is $D = 3 \pm 0.5$ pixels. The velocity field features only velocities in the *Y*-direction but a change in magnitude along the *X*-axis between the left and right sides of a shear zone is imposed (Fig. 8). The shape of the velocity profile across the shear zone is the error function, which means that the shear strain rate profile across the shear zone is a Gaussian curve.

4.2.1. Shear zone width

The incremental displacement on the right-hand side of the shear zone is set to 5 pixels, while on the left-hand side it is set to zero. The width of the shear zone (w_{sz}) was varied from 2000 to 30 pixels. The centre was positioned at 2000 pixels. The processing of the synthetic images with various PIV settings provided a good quantification of the position of the margins, and the velocity on either side. In agreement with the previous test, the largest interrogation window (now 128 pixels) together with overlap larger than 75% did smear sharp features such as shear zones narrower than 256 pixels (i.e. $w_{sz} < 2w_{ia}$). On the other hand, it resulted in the most precise, less noisy, measure of the velocity outside of the shear zone regardless of the shear zone width, and within the shear zone when the width is sufficiently large (i.e. $w_{sz} > 2w_{ia}$).

Also in agreement with the previous test, the noise increased with the window size decreased. For the employed particle density, a window size of 64 pixels is a reasonable lower limit, although with some filtering it remains possible to employ a window size of 32 pixels. We conclude that a window size of 128 to 64 pixels with overlap of 50–75% should provide the best result in
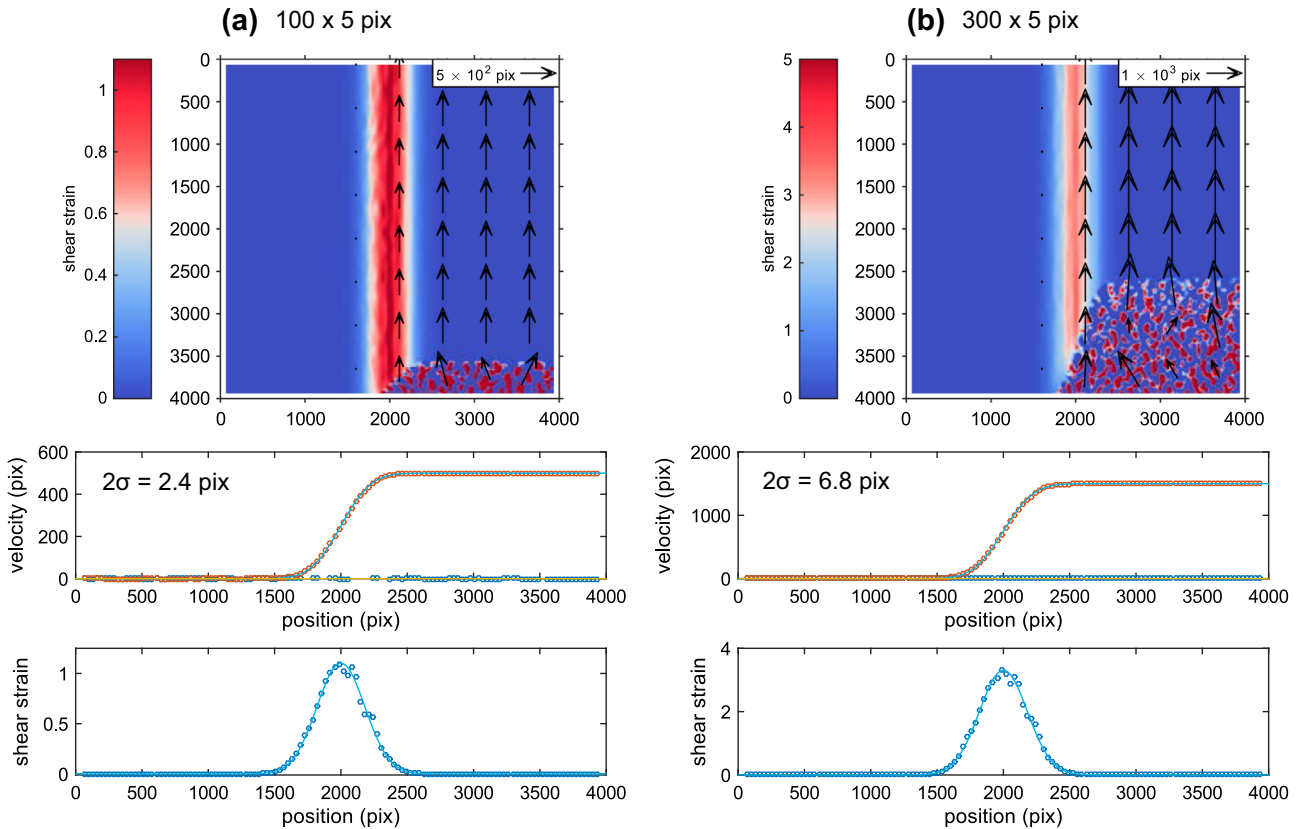

Fig. 11. Measurement of cumulative displacements and strain. The synthetic images, shear zone properties and correlation settings are identical to that of Fig. 10(d): $W_{ia} = 128$ pixels, $s = 32$ pixels. (a) Eulerian sum of 100 image pairs with incremental displacement of up to 5 pixels. The displacements are summed up and then the derivative is calculated. Both displacement and derivative match the imposed flow very well. (b) Eulerian sum of 300 image pairs. The PIV algorithm allows capturing large displacements (>1000 pixels) very accurately.
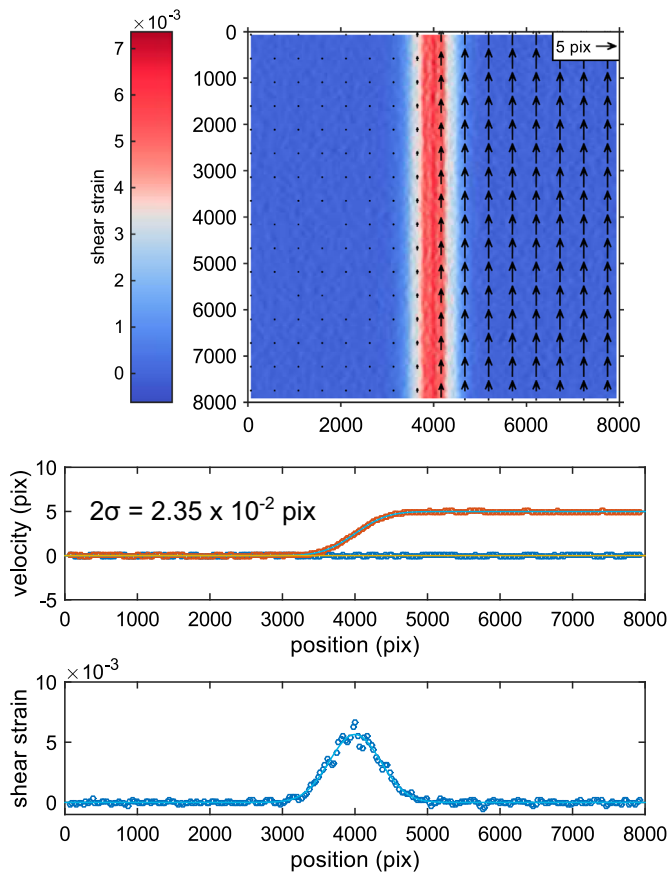
Fig. 12. Very large PIV image. Synthetic image 8000×8000 pixels with 1.8×10^7 particles ($\rho_p = 2.8 \times 10^{-1}$ pixels^{-2}) advected up to 5 pixels via a 2000 pixels-wide shear zone with normal shear strain distribution. Particle diameter is $D = 3 \pm 0.5$ pixels. Each image pair yield 61,009 vectors. The error of the velocity along the profile $Y = 4000$ pixels demonstrates accurate sub-pixel measurement across the very large domain. $W_{ia} = 128$ pixels, $s = 32$ pixels.

a variety of situations, provided the particle density is sufficient.

Finally, regardless of the window size, there is a minimum width of the shear zone that can be imaged. This is because the resolution of the final vector grid is associated with the size of the interrogation window. To have a high resolution vector grid without too much overlapping causing artificial smoothing, it is necessary to reduce the size of the interrogation window, which causes noise to increase as well.

This synthetic shear zone setup was also employed to calculate displacements using $V_r = 1$, 2, 10 or 15 pixels, and $V_l = 0$ with identical PIV settings. The algorithm was capable of measuring either large or small displacements. We also varied the displacement difference across the shear zone by progressively increasing V_r. However, as revealed by the good fit between imposed and recovered displacement and shear strain near the edges of the shear zone in Fig. 9b or d, the algorithm is capable of capturing small variations, and therefore changing V_r did not alter the outcome of the test.

4.2.2. Multipass

Here we test the advantage of the multipass approach using a large shear zone, the width of the shear zone is 1024 pixels and the displacement is 5 pixels. The synthetic images are correlated using several single pass approaches and compared to one multipass with similar window sizes. The first processing uses a large interrogation area of 128 pixels and step size of 64 pixels (i.e. 50% overlap). The result is a vector map with little error or noise but
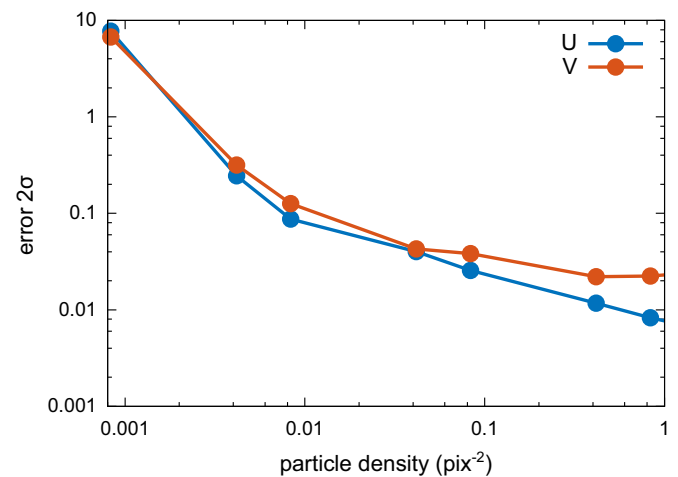

Fig. 13. Evolution of the error along a profile through a shear zone for various particle densities. The quality drops dramatically if the particle density is below 4.2×10^{-3} pixels^{-2}. $W_{sz} = 2000$ pixels, $D = 3 \pm 0.5$ pixels, $w_{ia} = 128$, $s = 32$ pixels.

only a few vectors inside the shear zone (Fig. 10a). The second processing employs a smaller interrogation area of 64 pixels and step of 32 pixels (i.e. 50% overlap). As a result of smaller step size, the number of vectors inside the shear zone is larger (Fig. 10b). However the smaller interrogation area produced higher noise reflected in larger error. Then we processed the same image using the previous two processing settings consecutively. The first pass employs a large interrogation window of 128 pixels which yields a vector grid interpolated to shift the smaller interrogation area in the second pass (Fig. 10c). The multipass does improve the resolution compared to the first pass and improve the quality compared to the second pass. However, the improvement is minimal while the processing time is significantly increased (Fig. 10c). An alternative is to use the smallest interrogation area which does not yield noise (here 128) and increase the overlap reasonably (here $s = 32$ pixels, overlap=75%). The velocity profile shows little noise and the strain profile confirms that the distribution of strain within the shear zone is well captured (Fig. 10d). We therefore suggest that a good setting for the employed particle density is an interrogation window of 128 pixels to provide precise measurement together with an overlap of 75% to obtain high resolution. If the shear zone is very narrow then the size of interrogation area should be reduced as our current multipass approach does not improve significantly the level of noise.

4.2.3. Cumulative deformation

It is crucial for experimental tectonics that the cumulative displacements and deformation are calculated accurately. Here we have employed the shear zone test and summed up a number of incremental displacements. Our shear zone set-up is suitable for an Eulerian sum since the deformation is self-similar along the strike of the shear zone. Fig. 11 shows the cumulative displacement across the shear zone when summing up to 300 vector fields. The advection of the particles leaves a growing gap behind where no particles can be found and therefore the vectors are erroneous. However elsewhere in the image the vectors are accurately summed up as the cumulative PIV displacement or shear strain closely match that employed for the synthetic images. It can be seen that the algorithm allows precisely locating the centre and edges of the shear zone, the quantity of displacement as well as the distribution of shear strain within the large shear zone, up to large strain (Fig. 11).

4.2.4. Very large images

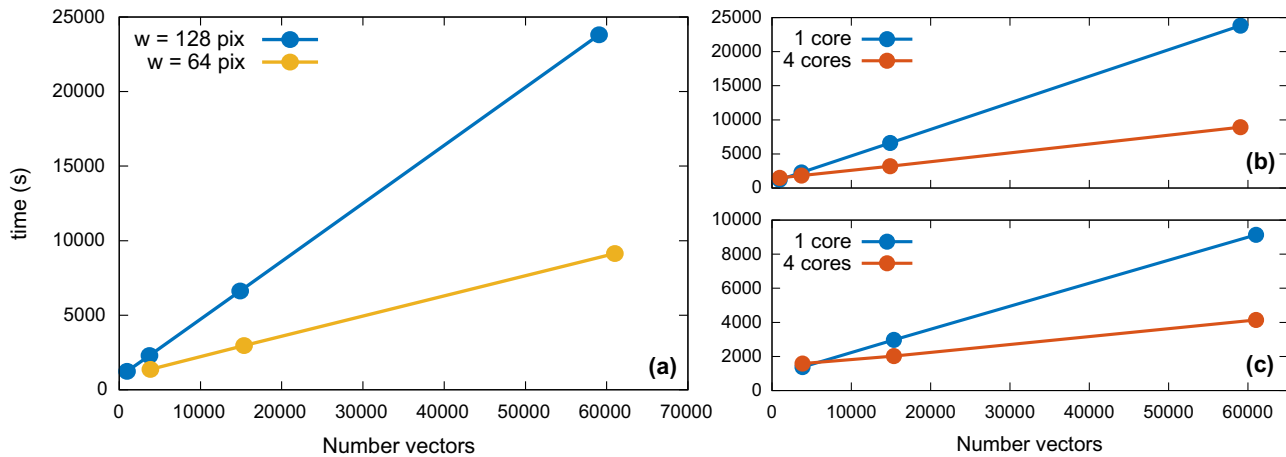The synthetic images generated to test the algorithm are

Fig. 14. Performance of correlation procedure. 301 images 4000 × 4000 pixels with 1024 pixels-wide shear zone in centre are employed. The velocity on the right-hand side of shear zone is 5 pixels. The images are not pre-processed, the region of interest is the full image, the universal outlier with kernel 3 × 3, $\epsilon = 0.15$ and threshold $K=2$ is employed. The discarded vectors are interpolated with a boundary solver. (a) Performance with one core, with interrogation window size of 128 or 64 pixels. The number of vectors is increased when reducing the step s between the vectors in the final grid (increase overlap). A larger window size demands more time. (b) Acceleration of procedure using a window of 128 pixels with 1 or 4 computation cores. (c) Acceleration of procedure using a window of 64 pixels with 1 or 4 computation cores.

significantly smaller than the images that can be obtained from modern DSLR (up to 50 Mpixels). However, since the algorithm is intended to process large images, it is important to demonstrate that the algorithm does work properly with larger images.

We created 105 large images (8000 × 8000 pixels) with 1.8×10^7 particles (i.e. $\rho_p = 2.8 \times 10^{-1}$ pixels^{-2}), created a large synthetic shear zone in the middle and correlated the successive images (Fig. 12). Using an interrogation area of 128 pixels and vector grid resolution of 32 pixels, each image pair provided 61,009 vectors yielding a very accurate quantification of displacement and shear distribution (Fig. 12). The correlation of each image pair took ∼150 s using a 12-cores workstation with 16 Gb memory.

4.2.5. Particle density

The noise increases when the size of the interrogation area is decreased. The larger the interrogation area, the higher the chance of the particle distribution being unique. However, this also depends on the number of particles in the image. We created a synthetic shear zone employed to advect particles in images with different particle densities, from 0.001 to 1 pixels^{-2}. The profile across the shear zone was employed to calculate the error in order to compare quantitatively the effect of particle density (Fig. 13). All but the lowest particle density provided vector maps which closely matched the flow field employed to generate the synthetic images. Therefore, qualitatively, the PIV algorithm worked for all particle densities larger than 4.2×10^{-3} pixels^{-2}. The error reduced for both the U and V velocity components but for particle densities greater than 4.1×10^{-1} pixels^{-2} the error on V flattened, while the error on U continued decreasing. This indicated that with too many particles the interrogation area becomes saturated with particles and therefore all the parts of the image start to become similar. The error reduction of the U component reflect the fact that we employed $U=0$, and start the correlation without offsets. For reference the pattern displayed in Fig. 4 obtained by sifting black particles on top of a wax model (e.g. Boutelier and Oncken, 2011) has a particle density of 8.85×10^{-3} pixels^{-2}, which was sufficient to calculate displacements.

4.2.6. Performance of cross-correlation

We employed the generated synthetic images of a shear zone with $W_{sz} = 1024$ pixels and $V_r=5$ pixels to measure the performance of the algorithm. We measure the time required to correlate up to 300 images for different PIV settings and different numbers of computation cores. We varied the size of the interrogation as well as the overlap. It is not surprising that increasing the overlap leads to many more vectors being calculated and therefore increases the computation time. Also not surprising is the fact that increasing the size of the interrogation area leads to an increase in computation time (Fig. 14a). Performing the same PIV analysis on the same images with 1 or 4 cores shows that the parallelization does accelerate the procedure, in particular for large images (Fig. 14b).

5. Future developments

The most important future development concerns the description of the mask which defines the region of interest (ROI) and may be updated using the incremental displacement vectors. We designed the initial ROI as a rectangle defined by the user. The vectors nearest to the edges of the rectangle are extracted and averaged. The velocity component perpendicular to each edge is calculated to advect it. Therefore the ROI always remains a rectangle. Although this does work for convergence or divergence imposed by a piston across the entire model width (e.g. models of subduction or rifting), it does not permit the mask to adapt to any along-strike variation of orthogonal velocity such as in our synthetic shear zone tests. The mask will have to be redefined to become a polygon able to adapt to such velocity variations.

A second current limitation is the calculation of the cumulative displacements. The current algorithm employs an Eulerian scheme. The vectors, which are summed up, are always in the same location. However, in tectonic modelling, we might be more interested in one particular object within the model, which is deformed and advected simultaneously. For example, what is the cumulative deformation accommodated by a rolling-back or advancing trench in a subduction model? To access this information a Lagrangian cumulation scheme needs to be developed.

A third limitation and future development rests in the correction of the experimental images. We employed a polynomial approach but a camera model has advantages. In particular, the camera model allows calibrating using a board which may be only a fraction of the image space, yet the whole image may then be calibrated, undeformed employed for correlation. The polynomial calibration may severely deform the image outside of the area

defined by the calibration board and therefore only this area can be used for the correlation.

Finally, we have removed the deformation of the interrogation area from the multipass correlation procedure of Thielicke and Stamhuis (2014) in order to parallelize and accelerate the processing of large images. However, the result is a multipass procedure which does not yield significant improvement, whereas Thielicke and Stamhuis (2014) have shown that with window deformation, the multipass approach does combine the best accuracy and resolution. We thus acknowledge that our current multipass approach is inferior and the window deformation will have to be implemented in the parallelized algorithm

6. Conclusions

We presented a new tool which facilitates the PIV analysis of experimental tectonics. The package allows importing a variety of raw images from DSLR through the use of the open DNG format. A procedure is described for the preprocessing of the experimental images via calibration and rectification. The correlation of successive views is parallelized and images are assembled displaying the model view with velocity vectors and spatial derivatives. Using synthetic tests we demonstrated that the software allows the use of large DSLR images to be employed and precise, high-resolution velocity vectors to be calculated. The PIV analysis of experimental tectonics provides the opportunity of precisely monitoring the distribution of strain in space and time, including low-strain which is too small to be included in mechanical analysis using more traditional methods. Therefore the presented software package allows for more constraints to be derived from analogue experiments and more robust conceptual models to be developed.

Acknowledgement

References

Adam, J., Urai, J., Wieneke, B., Oncken, O., Pfeiffer, K., Kukowski, N., Lohrmann, J., Hoth, S., van der Zee, W., Schmatz, J., 2005. Shear localisation and strain distribution during tectonic faulting—new insights from granular-flow experiments and high-resolution optical image correlation techniques. J. Struct. Geol. 27, 283–301.

Adrian, R., 1991. Particle-imaging techniques for experimental fluid-mechanics.

Annu. Rev. Fluid Mech. 23, 261–304.

Boutelier, D., Oncken, O., 2011. 3-D thermo-mechanical laboratory modeling of plate-tectonics: modeling scheme, technique and first experiments. Solid Earth 2, 35–51.

Buckingham, E., 1914. On physically similar systems; illustrations of the use of dimensional equations. Phys. Rev. 4, 345–376.

Corti, G., Bonini, M., Conticelli, S., Innocenti, F., Manetti, P., Sokoutis, D., 2003. Analogue modelling of continental extension: a review focused on the relations between the patterns of deformation and the presence of magma. Earth-Sci. Rev. 63, 169–247.

Graveleau, F., Malavieille, J., Dominguez, S., 2012. Experimental modelling of orogenic wedges: a review. Tectonophysics 538–540, 1–66.

Harris, C., Stephens, M., 1988. A combined corner and edge detector. In: Proceedings of the Alvey Vision Conference, pp. 147–151.

Hoth, S., Hoffmann-Rothe, A., Kukowski, N., 2007. Frontal accretion: an internal clock for bivergent wedge deformation and surface uplift. J. Geophys. Res. 112, B06408.

Hubbert, M.K., 1937. Theory of scale models as applied to the study of geologic structures. Geol. Soc. Am. Bull. 48, 1459–1519.

Jenkins, F.A., White, H.E., 1957. Fundamentals of Optics. McGraw-Hill, New York.

Koyi, H., 1997. Analogue modelling: from a qualitative to a quantitative technique a historical outline. J. Pet. Geol. 20, 223–238.

Le Corvec, N., Walter, T.R., 2009. Volcano spreading and fault interaction influenced by rift zone intrusions: insights from analogue experiments analyzed with digital image correlation technique. J. Volcanol. Geotherm. Res. 183, 170–182.

Leever, K.A., Gabrielsen, R.H., Sokoutis, D., Willingshofer, E., 2011. The effect of convergence angle on the kinematic evolution of strain partitioning in transpressional brittle wedges: insight from analog modeling and high-resolution digital image analysis. Tectonics 30, 1–25.

Lourenco, L.M., Krothapalli, A., Smith, C.A., 1989. Particle imaging velocimetry. In: Gad-el Hak, M. (Ed.), Advances in Fluid Mechanics Measurements. Lecture Notes in Engineering vol. 45. Springer Berlin Heidelberg, Berlin, Heidelberg, pp. 127–199 (Chapter 4), Lecture no edition.

Nobach, H., Honkanen, M., 2005. Two-dimensional Gaussian regression for sub-pixel displacement estimation in particle image velocimetry or particle position estimation in particle tracking velocimetry. Exp. Fluids 38, 511–515.

Pawlowicz, R., 2003. Quantitative visualization of geophysical flows using low-cost oblique digital time-lapse imaging. IEEE J. Ocean. Eng. 28, 699–710.

Raffel, M., Willert, C., Wereley, S., Kompenhans, J., 2007. Particle Imaging Velocimetry: A Practical Guide. Springer.

Ramberg, H., 1967. Model experimentation of the effect of gravity on tectonic processes. Geophys. J. R. Astron. Soc. 14, 307–329.

Ranalli, G., 2001. Experimental tectonics: from Sir James Hall to the present. J. Geodyn. 32, 65–76.

Schrank, C.E., Boutelier, D., Cruden, A.R., 2008. The analogue shear zone: from rheology to associated geometry. J. Struct. Geol. 30, 177–193.

Smith, S.W., 1999. The scientist and engineer's guide to digital signal processing. California Technical Publishing, San Diego CA.

Sterrett, S.G., 2009. Similarity and dimensional analysis. In: Meijers, A. (Ed.), Handbook of the Philosophy of Science. Philosophy of Technology and Engineering Sciences vol. 9. North-Holland, Amsterdam, pp. 799–823.

Taylor, Z.J., Gurka, R., Kopp, G.a., Liberzon, A., 2010. Long-duration time-resolved PIV to study unsteady aerodynamics. IEEE Trans. Instrum. Meas. 59, 3262–3269.

Thielicke, W., Stamhuis, E.J., 2014. PIVlab towards user-friendly, affordable and accurate digital particle image velocimetry in MATLAB. J. Open Res. Softw., 2.

Westerweel, J., Scarano, F., 2005. Universal outlier detection for PIV data. Exp. Fluids 39, 1096–1100.

Willert, C., Gharib, M., 1991. Digital particle image velocimetry. Exp. Fluids 193, 181–193.

Zhang, Z., 1999. Flexible camera calibration by viewing a plane from unknown orientations, in Proceedings of the seventh IEEE International Conference on Computer Vision. IEEE, Kerkyra 1, 666–673.